



The effect of chemical structure of carboxylate molecules on hydroxyapatite nanoparticles. A structural and morphological study

Lorenzo Degli Esposti^{a, **}, Alessio Adamiano^a, Dritan Siliqi^b, Cinzia Giannini^b, Michele Iafisco^{a, *}

^a Institute of Science and Technology for Ceramics (ISTEC), National Research Council (CNR), Via Granarolo 64, 48018, Faenza, Italy

^b Institute of Crystallography (IC), National Research Council (CNR), Via Amendola 122/O, 70126, Bari, Italy

ARTICLE INFO

Keywords:

Hydroxyapatite
Nanoparticles
Biom mineralization
Citrate
Carboxylates
Hydroxycitrate
Glutarate

ABSTRACT

Being the most abundant non-macromolecular organic component of bone, the role of citrate (Cit) in hydroxyapatite (HA) crystallization is of high relevance. In this work we have investigated the influence of hydroxycitrate (CitOH) and glutarate (Glr) on HA crystallization in terms of particle growth, composition, and morphology in comparison to Cit. CitOH and Glr have been selected for this work because they share the same backbone structure of Cit but bear different functional groups in the central region. Our data has revealed that CitOH strongly inhibits HA crystallization more efficiently than Cit. CitOH-HA nanoparticles are composed of platy, elongated particles similar to those of Cit-HA but they are ca. twice smaller and have a lower crystal order. On the other hand, Glr does not inhibit HA crystallization as Cit, but leads to the formation of OCP platelets that convert with maturation time to HA nanorods with larger aspect ratio than Cit-HA. In comparison to Cit-HA samples, Glr-HA nanoparticles have bigger dimensions, and higher structural order. Overall, our data reveal that the central carboxyl group of Cit is involved in the selective binding with HA crystal surface and in regulating HA crystal growth. The results of this work highlight new possibilities to control the formation of HA for designing advanced bioactive materials and give new insights on the role of the structure of Cit in regulating the HA morphology.

1. Introduction

Synthetic hydroxyapatite (HA) nanoparticles are nowadays widely employed for different technological sectors such as medicine, energy, environment, and many others [1–8]. Several preparation strategies have been set-up in the last years to tailor their properties [9–13]. Among them, the use of organic templates and additives is one of the most interesting methods to precisely control the structure and morphology of HA nanoparticles. Organic molecules act as templates by influencing the nucleation and growth of HA. This can be achieved both by the interaction of the template molecule with Ca^{2+} or PO_4^{3-} ions during nucleation, or by a preferential binding of the molecule towards specific HA crystal faces that inhibits their orthogonal growth [14–16].

In this regard it was demonstrated that citrate (Cit), which is a strong calcium chelating agent, is an efficient “bio-inspired” regulator of HA nanocrystals. Cit is involved in the growth of HA nanocrystals during

bone formation, and is present in a relatively great amount in bone tissue [17]. The influence of Cit on synthetic HA crystallization was widely studied, and it was shown that it has a double role (i) by inducing the formation of HA by direct conversion of an amorphous calcium phosphate precursor, and (ii) by prompting a non-classical growth of the particles by oriented aggregation [18–21]. HA prepared in presence of Cit (Cit-HA) possesses a platy needle-like shape, i.e., elongated nano-platelets. A well-accepted theory is that the citrates bind preferentially to HA (1 0 0) face, inhibiting its growth. As a consequence, crystals continue to grow in the other two orthogonal directions and the (1 0 0) crystal face becomes the main one. Furthermore, particles of Cit-HA undergo an oriented aggregation at the beginning of crystallization through the attachment the Cit-free (0 0 1) faces, that leads to an elongation of the crystals along the HA *c*-axis [21]. In addition, computational modeling has shown that if Cit molecules have a low concentration they prefer to attach to the HA surface in longitudinal orientation, stabilizing small HA nanocrystals with short lattice

Peer review under responsibility of KeAi Communications Co., Ltd.

* Corresponding author.

** Corresponding author.

E-mail addresses: lorenzo.degliesposti@istec.cnr.it (L. Degli Esposti), michele.iafisco@istec.cnr.it (M. Iafisco).

<https://doi.org/10.1016/j.bioactmat.2021.01.010>

Received 23 October 2020; Received in revised form 7 January 2021; Accepted 9 January 2021

2452-199X/© 2021 The Authors. Production and hosting by Elsevier B.V. on behalf of KeAi Communications Co., Ltd. This is an open access article under the CC

BY-NC-ND license (<http://creativecommons.org/licenses/by-nc-nd/4.0/>).

Abbreviations

Cit	citrate
CitOH	hydroxycitrate
FEG-SEM	field-emission gun scanning electron microscopy
FT-IR	Fourier-transform infra-red spectroscopy
Glr	glutarate
HA	hydroxyapatite
ICP-OES	inductively-coupled plasma optical emission spectroscopy
OCP	octacalcium phosphate
PXRD	powder X-ray diffraction
SAXS	small angle X-ray scattering
TGA	termogravimetric analysis

parameters; differently, when Cit concentration is high enough to cover the entire HA surface, the molecules are arranged with a parallel orientation, favoring the hydrogen bond connections between each pair of citrate molecule and the formation of much longer HA particles [22, 23]. Cit-HA nanoparticles are promising nanomaterials with a high degree of biomimeticism, high biocompatibility, and good stability in aqueous suspension [18] that have been used for several nanomedical applications [24,25]. In view of the high control that Cit can exert on HA nanoparticles, as well as its importance in bone biomineralization, the aim of this work is the synthesis and characterization of HA nanoparticles in presence of molecules which are chemically similar to Cit. In a previous work, the influence on HA formation of dicarboxylic acids with different chain length (i.e. oxalic acid, succinic acid, and adipic acid) was compared to citric acid [26]. Authors suggested that the inhibition of HA growth is mostly dependent on the dicarboxylic acid affinity for Ca^{2+} ions in solution as well as on the structural/steric effect of the molecules [26].

In the present work, HA was synthesized using as templates two carboxylate molecules that share the same carbon backbone structure of Cit, that is to say two carboxylic groups separated by three carbon atoms but bear different functional groups in the central region, i.e. hydroxycitrate (CitOH), that possesses one extra hydroxyl group, and glutarate (Glr), that lacks one carboxyl and hydroxyl group in respect to Cit (Fig. 1). Although being structurally similar to Cit, CitOH was found to have a different crystal face selectivity towards calcium oxalate [27] and dicalcium phosphate dihydrate (DCPD, $\text{CaHPO}_4 \cdot 2\text{H}_2\text{O}$) [28], and to be a stronger growth inhibitor due to the increased hydrogen bonding to mineral surface [27,28]. In addition, CitOH was proposed as alternative to Cit as kidney stone prevention agent due to its stronger growth inhibition effect on calcium oxalate crystals [27]. However, to the best of our knowledge the influence of CitOH on HA crystal growth has never been studied.

Glr was used to control HA growth only in hydrothermal crystallization conditions, where it was proved to be associated to surface water molecules and to drive the growth via a crystalline precursor [29]. Nevertheless, the influence of Glr on the HA formation in non-hydrothermal conditions was never reported.

Herein, HA nanoparticles were prepared through a thermal-decomplexing batch reaction [18,30] using these carboxylate

molecules as Ca^{2+} complexing agents, and the physico-chemical, morphological, and surface properties of the obtained HA nanoparticles upon different maturation times have been characterized by conventional analytical techniques as well as by synchrotron-light small-angle X-ray scattering (SAXS).

2. Materials and methods**2.1. Materials**

The following reagents were used: glutaric acid ($\text{C}_5\text{H}_8\text{O}_4$, $\geq 99.0\%$, $\text{H}_2(\text{Glr})$, Sigma-Aldrich), potassium hydroxycitrate tribasic monohydrate ($\text{K}_3(\text{C}_6\text{H}_5\text{O}_8) \cdot \text{H}_2\text{O}$, $\geq 95.0\%$, $(\text{K}_3(\text{CitOH}))$, Sigma-Aldrich), sodium citrate tribasic dihydrate ($\text{Na}_3(\text{C}_6\text{H}_5\text{O}_7) \cdot 2\text{H}_2\text{O}$, $\geq 99.0\%$, $(\text{Na}_3(\text{Cit}))$, Sigma-Aldrich), sodium hexametaphosphate ($(\text{NaPO}_3)_6$, $\geq 96.0\%$, Sigma-Aldrich), sodium hydroxide (NaOH , $\geq 99.0\%$, Sigma-Aldrich), sodium phosphate dibasic dihydrate ($\text{Na}_2\text{HPO}_4 \cdot 2\text{H}_2\text{O}$, $\geq 99.0\%$, Sigma-Aldrich), and calcium chloride dihydrate ($\text{CaCl}_2 \cdot 2\text{H}_2\text{O}$, $\geq 99.0\%$, Sigma-Aldrich). All the solutions were made with ultrapure water (Arium pro, Sartorius).

2.2. Sample preparation

Carboxylate-HA nanocrystals were prepared by a wet precipitation method derived from the one developed by Delgado-López et al. [18]. The precipitation was initiated by mixing two solutions at room temperature (100 mL each). The first solution contained CaCl_2 100 mM + X 400 mM (where X is $\text{Na}_3(\text{Cit})$, $\text{H}_2(\text{Glr})$, or $\text{K}_3(\text{CitOH})$), while the second solution contained Na_2HPO_4 120 mM. The calcium containing solution was basified with NaOH to reach pH 8.5 before the mixing. Subsequently, the mixture was placed in a silicone oil bath at 80 °C and kept under stirring for different maturation times (5 min, 2 h, 4 h, 16 h and 24 h). After maturation the particles were separated from the mother liquor by centrifugation at 7000 RPM for 10 min, washed with ultrapure water by several resuspension and centrifugation steps, and then freeze-dried overnight. Afterward, the obtained powders were manually ground and sieved (mesh size: 270) in order to achieve homogeneous granulometry. All samples preparations were performed in triplicate, as well as all characterizations. The data are expressed as mean value \pm standard deviation.

2.3. Structural, chemical, and morphological characterization

The activity of the aqueous species as a function of temperature and pH as well as the saturation indexes of solid products were calculated with the Visual MINTEQ 3.1 software [31].

Powder X-ray diffraction (PXRD) patterns were acquired with a D8 Advance diffractometer (Bruker, Karlsruhe, Germany). PXRD patterns were collected in the angular range from 10 to 80° 2 θ with a step size of 0.02° and an acquisition time of 1s using Cu K α radiation ($\lambda = 1.54178$ Å) generated at 40 kV and 40 mA. A standard LaB₆ sample was collected with the same instrumental setup.

HA unit cell was indexed with FullProf program [32]. As initial screening, the PXRD pattern of Cit-HA at 2 h of maturation was modeled through Rietveld refinement both with a hexagonal [33] or a monoclinic HA structure [34]. After this initial evaluation, the unit cell parameters of all the samples were extracted as single-phase by Rietveld refinement

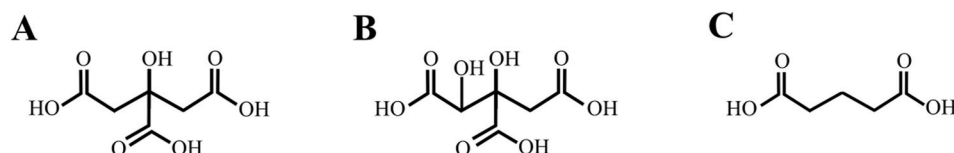


Fig. 1. Molecular structure of (A) citric acid, (B) hydroxycitric acid, and (C) glutaric acid.

using tabulated atomic coordinates of hexagonal HA [33]. In the case of Glr-HA sample at 5 min of maturation (Glr-HA 5 m), a multi-phase PXRD pattern refinement was executed. The relative content and unit cell parameters of OCP and HA were refined as a biphasic system starting from tabulated atomic positions (HA: PDF card 00-009-0432, OCP: PDF card 00-026-1056) [35,36]. For all refinements the peak broadening was modeled with spherical harmonics, and patterns background was calculated through the Chebychev function (11th order polynomial).

The dimensions of crystalline domains along HA (002) and (020) directions ($D_{[002]}$ and $D_{[020]}$) were calculated from the full-profile peak broadening analysis with the software FullProf [32], accounting for instrumental peak broadening effect measured on the standard LaB₆ sample (see details in Ref. [37]). The crystallinity of the samples was evaluated as reported by Wei et al. [38] with the use of the crystallinity index $X_c = 1 - (V_{112/300}/I_{300})$, where $V_{112/300}$ is the intensity of the angular region between HA (1 1 2) and (3 0 0) peaks and I_{300} is the intensity of HA (3 0 0) peak.

Fourier transform infrared (FT-IR) spectra of the samples were measured with a Nicolet iS5 spectrometer (Thermo Fisher Scientific Inc., Waltham, MA, USA) by using the KBr pellet method. Instrumental resolution was set up to 4 cm⁻¹, and 32 scans were collected per sample.

Scanning electron microscopy (SEM) micrographs of the samples were collected with a field-emission microscope (FEG-SEM, mod. SIGMA, ZEISS NTS GmbH, Oberkochen, Germany). The samples were dispersed in 10 mL of a 0.003 wt% (NaPO₃)₆ solution at a concentration of 0.05 mg mL⁻¹ and sonicated under ice cooling with a Vibracell VCX 500 tip sonicator (SONICS, Newtown, CT, USA) at 20% amplitude for 3 min with a pulsation of 5 s. Subsequently, the nanoparticles dispersion was dropped on a polished silicon wafer attached to a SEM stub and left to dry completely. Afterward, the samples were coated with 2 nm of Pt/Pd alloy using a Polaron E5100 sputter-coater (Polaron Equipment, Watford, Hertfordshire, UK). FEG-SEM working parameters were: 3 kV acceleration voltage, 1.8 mm working distance, in-lens acquisition mode.

Elemental quantification was performed with an Agilent Technologies 5100 inductively-coupled plasma atomic emission spectrometer (ICP-OES) (Agilent Technologies, Santa Clara, CA, USA). Sample preparation consisted in dissolving the powdered materials at a concentration of 0.2 mg mL⁻¹ in 50 mL of 1 wt% HNO₃ aqueous solution.

Thermogravimetric analysis of the samples (TGA) was carried out with a STA 449F3 Jupiter device (Netzsch GmbH, Selb, Germany). Thermograms were collected from room temperature to 1100 °C with a ramp of 10 °C min⁻¹ under air flow using an alumina pan.

ζ-Potential of the samples was measured with a Zetasizer Nano ZSP analyzer (Malvern, UK). The samples were dispersed in water at a concentration of 0.5 mg mL⁻¹ and the ζ-potential at spontaneous pH was measured using DTS1061 cells (Malvern, UK) at 25 °C.

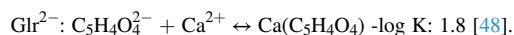
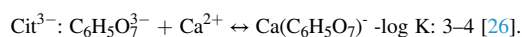
Small Angle X-ray Scattering (SAXS) curves of the samples were recorded at the Austrian SAXS beamline of the ELETTRA Synchrotron (Trieste, Italy) [71]. Incident beam energy was set up at 8 keV and allowed to measure the curve from a q-value of 0.08 to ca. 6 nm⁻¹. The sample holder was a ∅ 1.5 mm glass capillary (WJM-Glas Müller GmbH, Berlin-Pankow, DE). Before sample analysis, the background curve was acquired as the scattering at room temperature from the empty sample holder. A 2D scattering image was collected with a Pilatus 1 M detector (Dectris, CH), and therefore the 2D image was circularly averaged to be converted into a conventional SAXS curve. This step was performed with the software Fit2D available at the beamline [39]. Ten SAXS curves were acquired and averaged per sample, and therefore the background was removed with the software Igor Pro (WaveMetrics, Inc., Lake Oswego, OR, USA). The SAXS data analysis and the modeling was performed with the ATSAS package V3.0.2 [40]. and SasView package V4.2.2 (www.sasview.org). Schulz distribution was used to estimate the averaged particle size as well as the polydispersity of the samples for selected structural models [41,42,72]. SAXS data modeling was performed either with a lamellar model [43], as well as with an elliptical cylinder model [44].

3. Results and discussion

3.1. Carboxylate molecules speciation and evaluation of their interaction with calcium ions

HA nanoparticles in presence of carboxylate molecules were prepared by a thermal decomplexing batch reaction which was already used in a previous work for the preparation of Cit-HA [18,20,21,30]. It was reported that in the reaction environment, Cit complexes Ca²⁺ ions and forms a homogeneous metastable solution at pH > 8.3, that avoids the instantaneous nucleation and precipitation of calcium phosphate. In addition, at pH > 8 citrate is completely deprotonated as Cit³⁻ and it strongly interacts with HA nuclei, forming a highly negative surface charge that prevents particle aggregation [22,45]. With the increase of temperature, the Cit-Ca complex is destabilized and a gradual and homogeneous decomplexation occurs leading to the release of Ca²⁺ ions and the formation of HA with Cit. In order to evaluate the influence of CitOH and Glu on HA crystallization in comparison to Cit, the calcium complexing efficacy of the three carboxylates was compared. For this purpose, first, the predominant species in solution for each carboxylate were analyzed as a function of pH. The carboxylates have multiple dissociation equilibria; the equilibrium reactions for Cit, CitOH, and Glr and the corresponding dissociation constants (pKa) are listed in Table 1. On the basis of the pKa values and speciation simulations, at the reaction pH (8.5) all the three carboxylates are completely dissociated and only the forms Cit³⁻, CitOH³⁻, and Glr²⁻ are present in solution [46].

The affinity of these carboxylate ions toward Ca²⁺ ions were then estimated on the basis of previously reported literature data. For the sake of simplicity, only the calcium-binding constants of the dissociated anionic forms (i.e., Cit³⁻ and Glr²⁻) present in the reaction conditions are reported. The calcium-binding constants are the following:



To the best of our knowledge, the calcium binding constant of CitOH³⁻ has never been reported. However, Chung et al. [27] calculated the Ca-carboxylate complex binding energy in vacuum for Cit and CitOH, and have proven that CitOH has a stronger affinity for Ca²⁺ in comparison to Cit. Hence, the three carboxylates have different complexation strengths toward calcium ions, that is to say CitOH > Cit > Glr. Indeed, a higher complex stability would generate a lower concentration of free Ca²⁺ ions in solution and thus reduce supersaturation and nucleation rates. Furthermore, as reported in a previous work [26] a higher Ca-carboxylate complex strength could induce a higher binding of carboxylate molecules on HA crystals, inhibiting crystal growth.

The activities of the species in the reaction mixture as function of

Table 1
Speciation reactions and dissociation constants for Cit, CitOH and Glr.

Cit	pKa ^a
$\text{C}_6\text{H}_8\text{O}_7 \leftrightarrow \text{C}_6\text{H}_7\text{O}_7^-$	3.13
$\text{C}_6\text{H}_7\text{O}_7^- \leftrightarrow \text{C}_6\text{H}_6\text{O}_7^{2-}$	4.76
$\text{C}_6\text{H}_6\text{O}_7^{2-} \leftrightarrow \text{C}_6\text{H}_5\text{O}_7^{3-}$	6.40
CitOH	pKa ^b
$\text{C}_6\text{H}_8\text{O}_8 \leftrightarrow \text{C}_6\text{H}_7\text{O}_8^-$	2.90
$\text{C}_6\text{H}_7\text{O}_8^- \leftrightarrow \text{C}_6\text{H}_6\text{O}_8^{2-}$	4.29
$\text{C}_6\text{H}_6\text{O}_8^{2-} \leftrightarrow \text{C}_6\text{H}_5\text{O}_8^{3-}$	5.11
Glr	pKa ^b
$\text{C}_5\text{H}_6\text{O}_4 \leftrightarrow \text{C}_5\text{H}_5\text{O}_4^-$	3.76
$\text{C}_5\text{H}_5\text{O}_4^- \leftrightarrow \text{C}_5\text{H}_4\text{O}_4^{2-}$	4.56

^a Dissociation constants from Martell and Smith [47].

^b Dissociation constants from ChemAxon.

temperature were calculated and plotted in Fig. 2 [18]. In the case of Glr, the Ca-Glr complex ($[\text{Ca}(\text{Glr})]$) is destabilized and decreases in activity with the increase of temperature (Fig. 2) similarly to the Ca-Cit complex ($[\text{Ca}(\text{Cit})]$). Therefore, Glr presents a behavior similar to Cit where the heating leads to a gradual thermal decomplexation and release of Ca^{2+} ions into the solution. The progressive release of Ca^{2+} in presence of PO_4^{3-} induces the formation of calcium phosphate ions, such as $[\text{CaPO}_4]^-$, followed by the formation of calcium phosphate precipitates. However, the $[\text{Ca}(\text{Glr})]$ has a lower activity in comparison to the $[\text{Ca}(\text{Cit})]$ complex, as consequence of the lower calcium complexation strength of Glr. This leads to a higher activity of free Ca^{2+} and Glr^{2-} ions and also of $[\text{CaPO}_4]^-$ species, implying that in presence of Glr the precipitation of calcium phosphate should be more intense. Indeed, this was confirmed also by the calculation of the saturation indexes of the possible solid products for the reaction mixtures in presence of Glr or Cit (Table S1) performed by Visual MINTEQ. It was calculated that for both the carboxylates, the highest supersaturated minerals are HA followed by octacalcium phosphate (OCP, $\text{Ca}_8\text{H}_2(\text{PO}_4)_6 \cdot 5\text{H}_2\text{O}$). The reaction mixture with Glr presents the highest saturation indexes for both HA and OCP in comparison to Cit, suggesting that solid phases precipitation should be faster than in Cit reaction mixture. Overall, these calculations suggest that Glr could be used for a thermal-decomplexing precipitation of HA, but its lower complex strength for Ca^{2+} should lead to a faster precipitation and a lower crystal growth inhibition in respect to Cit. The thermodynamic parameters of CitOH are not available, thus, the

Ca-CitOH activities were not calculated. However, taking into account the structural similarity between Cit and CitOH together with the higher Ca-CitOH complex strength in comparison to Ca-Cit, we hypothesize that Ca-CitOH could have a thermal-decomplexing behavior similar to Ca-Cit, but with higher activity and a lower destabilization by temperature increase.

It must be taken into account that the concentration of the carboxylate molecules can influence the carboxylate- Ca^{2+} complex stability and thus could affect HA size, morphology and crystallinity. In this work we have used the same concentration for all the carboxylates tested in order to study the influence of their structure on HA crystallization. Future studies will be dedicated to elucidate the effect of Cit, Glr and CitOH concentration on the nucleation and growth of HA nanoparticles.

3.2. PXRD characterization

PXRD patterns of CitOH-HA, Glr-HA, and Cit-HA samples indicate HA (powder diffraction file 00-009-0432) as the only phase present for all samples collected at every maturation time (Fig. 3A–C), with the exception of Glr-HA 5 m (see below). All the samples display PXRD patterns with broad diffraction peaks, indicating that the materials are composed by nanocrystals [18]. The PXRD patterns of all the samples after 5 min of maturation show very broad peaks, that become progressively sharper at longer maturation time.

The increase of peak resolution upon maturation corresponds to an

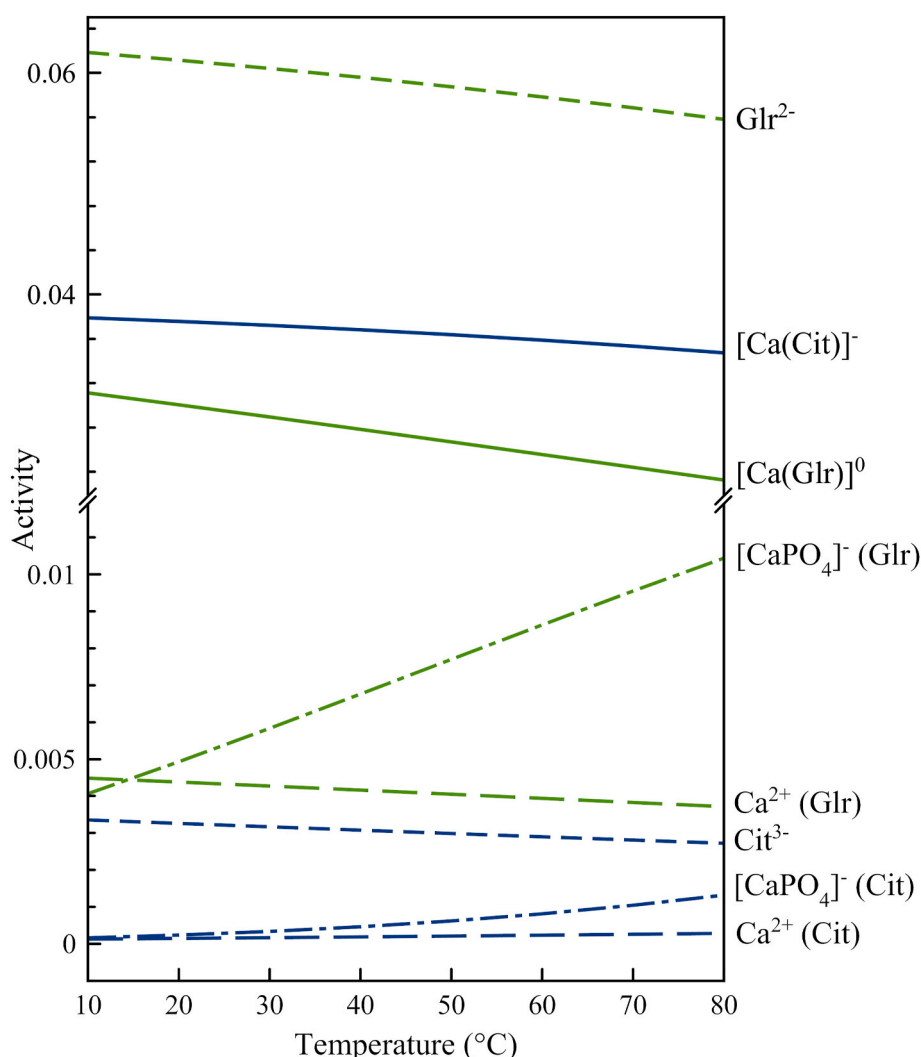


Fig. 2. Calculated activities, as a function of temperature, of the main ionic and neutral species in Glr and Cit reaction mixture (pH 8.5).

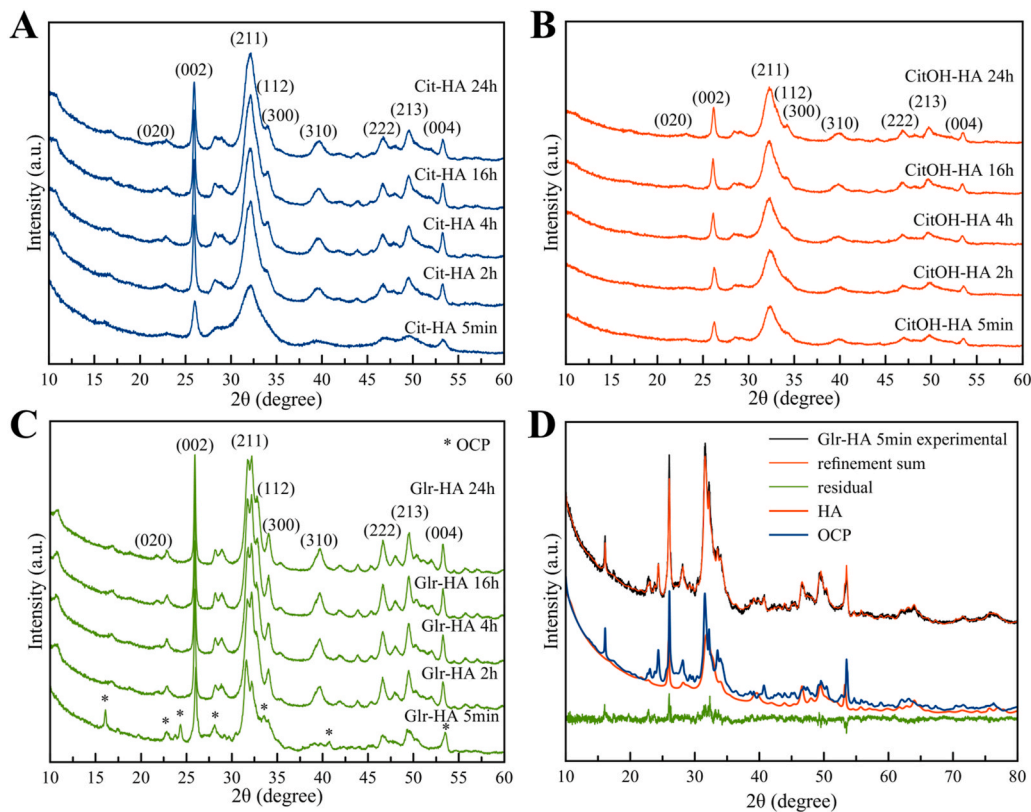


Fig. 3. PXRD patterns of (A) Cit-HA, (B) CitOH-HA, and (C) Glr-HA at 5 m, 2h, 4h, 16h, 24h of maturation time. (D) Multiphase Rietveld refinement of Glr-HA 5min.

increase of HA structural order and crystal growth. The peaks of the PXRD patterns of Glr-HA samples are sharper than those of Cit-HA samples for all time points, indicating that the crystalline domains of Glr-HA samples are larger and more ordered than those of Cit-HA. Moreover, the PXRD pattern of Glr-HA 5 m (Fig. 3C) presents some differences in comparison to both Cit-HA 5 m and CitOH-HA 5 m. In this sample, in addition to HA peaks, other signals are visible indicating the presence of octacalcium phosphate (OCP, $\text{Ca}_8\text{H}_2(\text{PO}_4)_6 \cdot 5\text{H}_2\text{O}$, powder diffraction file 00-026-1056, marked with * in Fig. 3C). Quantitative phase analysis, based on Rietveld whole profile fitting (Fig. 3D), confirmed this finding, and evidenced that Glr-HA 5 m was composed by 55.0 ± 0.4 wt% HA and 45.0 ± 0.2 wt% OCP ($R_{\text{wp}} = 12.3$). On the other hand, the PXRD patterns of CitOH-HA samples are similar to those of Cit-HA, both reporting the typical features of HA.

It was observed that HA precipitated in absence of carboxylates in reaction conditions similar to those used in this work crystallizes via an OCP precursor phase [20,21]. On the other hand, previous works on Cit-HA have shown that Cit-HA is formed by conversion of an amorphous precursor without passing through metastable crystalline phases [21]. The formation of OCP as precursor of HA was also previously reported for a Glr-HA prepared by a hydrothermal process [29]. By comparing the rate of OCP to HA conversion of Glr-HA and of HA prepared in similar conditions without carboxylates it can be observed that Glr accelerates the OCP to HA conversion. In fact, in a previous work OCP was still present after 4 h of maturation [20], while for our Glr-HA sample OCP disappears after 2 h of maturation. This result suggests that the formation of HA in presence of Glr seems to follow the Ostwald's rule of phases in agreement with literature data, and the presence of Glr accelerates the conversion of OCP to HA.

Although crystalline HA possess a hexagonal $\text{P6}_3/\text{m}$ structure, also a monoclinic $\text{P2}_1/\text{b}$ structure has been proposed [34]. This monoclinic structure was observed in biogenic HA [49] and it was proposed also for platelet-shaped Cit-HA nanoparticles [20]. For this reason, we have used both HA structures to refine Cit-HA 2h sample. While both structures fit

well the experimental data (Figure S1), the hexagonal one gives the best fitting (χ^2 hexagonal: 1.43; χ^2 monoclinic: 1.64) and therefore was used

Table 2

Unit cell parameters and crystalline domain sizes of the samples.

Sample	a - b cell axes (Å)	c cell axis (Å)	$D_{(002)}$ (nm)	$D_{(020)}$ (nm)	$D_{(002)}/$ $D_{(020)}$
Cit-HA 5 m	9.510 ± 0.005	6.854 ± 0.005	9.7 ± 1.0	2.2 ± 1.0	4.4 ± 2.0
Cit-HA 2h	9.435 ± 0.005	6.872 ± 0.005	22.8 ± 1.0	4.9 ± 1.0	4.7 ± 1.0
Cit-HA 4h	9.434 ± 0.005	6.871 ± 0.005	30.1 ± 1.0	6.6 ± 1.0	4.6 ± 0.7
Cit-HA 16h	9.434 ± 0.005	6.871 ± 0.005	31.0 ± 1.0	6.6 ± 1.0	4.7 ± 0.7
Cit-HA 24h	9.435 ± 0.005	6.866 ± 0.005	27.4 ± 1.0	7.9 ± 1.0	3.5 ± 0.5
CitOH-HA 5 m	9.432 ± 0.005	6.864 ± 0.005	22.0 ± 1.0	6.3 ± 1.0	3.5 ± 0.6
CitOH-HA 2h	9.428 ± 0.005	6.863 ± 0.005	17.5 ± 1.0	4.6 ± 1.0	3.8 ± 0.9
CitOH-HA 4h	9.428 ± 0.005	6.863 ± 0.005	21.0 ± 1.0	5.6 ± 1.0	3.8 ± 0.7
CitOH-HA 16h	9.447 ± 0.005	6.879 ± 0.005	25.2 ± 1.0	7.1 ± 1.0	3.5 ± 0.5
CitOH-HA 24h	9.428 ± 0.005	6.863 ± 0.005	22.8 ± 1.0	6.9 ± 1.0	3.3 ± 0.5
Glr-HA 5 m	9.471 ± 0.005	6.866 ± 0.005	23.5 ± 1.0	5.0 ± 1.0	4.7 ± 1.0
Glr-HA 2h	9.452 ± 0.005	6.875 ± 0.005	39.2 ± 1.0	8.8 ± 1.0	4.5 ± 0.5
Glr-HA 4h	9.451 ± 0.005	6.876 ± 0.005	40.9 ± 1.0	9.4 ± 1.0	4.4 ± 0.5
Glr-HA 16h	9.450 ± 0.005	6.875 ± 0.005	46.7 ± 1.0	10.3 ± 1.0	4.5 ± 0.5
Glr-HA 24h	9.445 ± 0.005	6.874 ± 0.005	40.6 ± 1.0	9.8 ± 1.0	4.1 ± 0.4

to model all the samples. The unit cell parameters of the samples fitted by Rietveld refinement of PXRD data are reported in Table 2. The unit cell parameters of all the samples slightly shrink upon maturation [24]. However, the unit cell parameters of CitOH-HA 16h sample are slightly out of trend; we hypothesize that this discrepancy is probably due to experimental variability. The cell parameters of Cit-HA reported here are in agreement with the literature [20], and are comparable to those of CitOH-HA and Glr-HA. The size of HA crystalline domains along the non-overlapped [0 0 2] and [0 2 0] crystallographic directions are listed in Table 2. In addition, the crystallite shape of the samples after 24 h of maturation is reported in Figure S2. With the exclusion of the samples after 5 min of maturation, the size of the crystalline domains of Glr-HA along the *c*-axis ($D_{(002)}$) and along the *b*-axis ($D_{(020)}$) are both larger than those of Cit-HA, which in turn are larger than those of CitOH-HA. The crystalline domains slightly increase upon maturation for all carboxylate-HA samples. For all materials the $D_{(002)}$ values are higher than the corresponding $D_{(020)}$ values, demonstrating that all nanocrystals are extended along *c*-axis. The crystalline domains aspect ratio $D_{(002)}/D_{(020)}$ is similar for Glr-HA and Cit-HA and is higher than CitOH-HA, irrespectively of the maturation time. Finally, the crystallinity index of the samples (Table S2) confirm that Glr-HA is more crystalline than Cit-HA and CitOH-HA independently from maturation time, and the crystallinity of the samples improves with maturation time. Crystallographic data show that in terms of crystalline domains size, crystalline order, and crystallinity Glr-HA > Cit-HA > CitOH-HA at all maturation times. The PXRD data of CitOH-HA confirm that CitOH has a stronger HA crystal growth inhibition effect than Cit, as previously reported for DCPD and calcium oxalate [27,28].

Table 3
Chemical composition and ζ -potential of the samples.

Sample	Ca/P ^a	Carboxylate molecule ^b (wt.%)	Structural water ^b (wt.%)	ζ -potential ^c (mV)
Cit-HA 5 m	1.54 ± 0.02	2.0 ± 0.2	4.1 ± 0.4	-15.5 ± 0.6
Cit-HA 2h	1.53 ± 0.02	1.9 ± 0.2	2.9 ± 0.3	-13.4 ± 0.3
Cit-HA 4h	1.53 ± 0.01	1.6 ± 0.2	3.0 ± 0.3	-15.8 ± 0.5
Cit-HA 16h	1.48 ± 0.01	1.5 ± 0.1	3.3 ± 0.3	-17.1 ± 0.3
Cit-HA 24h	1.53 ± 0.02	1.5 ± 0.2	2.5 ± 0.3	-16.5 ± 0.3
CitOH-HA 5 m	1.74 ± 0.07	9.4 ± 0.9	6.9 ± 0.7	-34.6 ± 0.5
CitOH-HA 2h	1.75 ± 0.02	8.5 ± 0.9	7.9 ± 0.8	-33.9 ± 0.9
CitOH-HA 4h	1.45 ± 0.04	6.4 ± 0.6	6.9 ± 0.7	-35.1 ± 1.0
CitOH-HA 16h	1.50 ± 0.03	4.1 ± 0.1	6.1 ± 0.6	-33.2 ± 0.7
CitOH-HA 24h	1.52 ± 0.02	2.8 ± 0.3	7.6 ± 0.8	-34.5 ± 0.3
Glr-HA 5 m*	1.30 ± 0.01	1.7 ± 0.2	3.6 ± 0.4	-1.9 ± 0.2
Glr-HA 2h	1.42 ± 0.01	0.7 ± 0.1	0.9 ± 0.1	-1.5 ± 0.1
Glr-HA 4h	1.43 ± 0.01	0.4 ± 0.1	0.9 ± 0.1	-2.3 ± 0.4
Glr-HA 16h	1.44 ± 0.01	0.6 ± 0.1	1.6 ± 0.1	-3.9 ± 0.4
Glr-HA 24h	1.45 ± 0.03	0.4 ± 0.1	1.4 ± 0.1	-5.7 ± 0.4

^(a) Quantified by ICP-OES; ^(b) Quantified by TGA; ^(c) Measured by DLS.

* Glr-HA 5 m chemical composition is influenced by the presence of OCP phase.

3.3. Compositional analysis

Chemical composition and ζ -potential values of the materials are listed in Table 3. The Ca/P molar ratio of Glr-HA samples (ca. 1.4) is slightly lower than the one of Cit-HA samples (approx. 1.5), and for both the materials it is lower than the Ca/P ratio of stoichiometric HA (i.e. 1.67), that indicates that the Glr-HA and Cit-HA samples are Ca-deficient. Ca/P ratio of Glr-HA 5 m is not comparable to the other Glr-HA samples because is a biphasic material. The Ca/P ratio of Glr-HA and Cit-HA does not change upon maturation. On the other hand, the Ca/P ratio of CitOH-HA at early maturation time (ca. 1.75) is the highest among the samples tested and decreased upon maturation to a value similar to Cit-HA. The high values of Ca/P of CitOH-HA samples at low maturation times are particularly interesting, because a Ca/P ratio higher than 1.67 is not common for materials that do not possess phosphate-substituting anions. It is likely that at early maturation times the high content of CitOH (see below) and the high Ca-CitOH complex strength induces the formation of a calcium-rich surface layer composed of non-soluble Ca-CitOH complexes [45]. The presence of these complexes on the nanoparticles surface can hinder the crystal growth, and thus could be the cause of the limited crystallization of CitOH-HA samples.

All the samples contain a limited amount of carboxylate and carbonate ions together with structural water molecules, which were measured by TGA-DTG (Figure S3) [50]. Carbonate ions incorporated in carboxylate-HA samples are due to atmospheric CO₂ dissolved in the solution during the precipitation. The term “structural water” refers to tightly bound water molecules, which are removed only by heating the materials at temperatures higher than 200 °C, that are not comprised in HA stoichiometry but are included in a non-apatitic hydrated outer layer present in freshly formed HA [51]. With maturation and development of crystal order, the non-apatitic hydrated surface layer progressively dissolves and the amount of structural water decreases. Therefore, structural water content is an indirect indicator of nanoparticles maturation.

Glr-HA has a lower content of carboxylate and structural water than Cit-HA at every time point. Glr content in Glr-HA samples decreases during the first 2 h of maturation and then remains stable, while in Cit-HA samples the amount of Cit and structural water constantly decreases up to 24 h due to the progressive dissolution of the hydrated outer layer [18]. In comparison, the low decrease over time of Glr and water content in Glr-HA complies with the complete dissolution of the hydrated surface layer at early crystallization times. Interestingly CitOH-HA has a higher content of carboxylate, and structural water at every maturation time in comparison to Cit-HA and Glr-HA. CitOH content constantly decreases up to 24 h of maturation time, while the structural water content remains constant. The high content of structural water and carboxylate molecules of CitOH-HA at high maturation time suggests that in this case the crystalline phase of HA is less developed, and moreover the non-apatitic hydrated surface layer might still be present. Overall, the carboxylate content of the samples is in agreement with the binding affinity of the molecules for calcium ions.

The ζ -potential values of all samples in aqueous solution at spontaneous pH (about 7.0) are negative, and this is caused by the carboxylate anions on HA surface [52]. Glr-HA surface charge is always less negative than Cit-HA (ca. -6 mV vs ca. -17 mV), while the surface charge of CitOH-HA is more negative than Cit-HA (ca. -34 mV vs ca. -17 mV). According to Ivachenko et al. and Hu et al., when Cit is adsorbed on HA surface it exposes outside its apolar central region, thus making HA surface more hydrophobic [17,53]. Therefore, in CitOH-HA the presence of the additional hydroxyl group generates a more charged surface as evinced by the ζ -potential data, while on the other hand in Glr-HA the lack of the central carboxyl group of Glr in comparison to Cit leads to a more neutrally charged surface. However, it must be taken into account that the three carboxylates have also a different relative abundance on HA surface due to their different binding strength toward HA, which in turn influences the ζ -potential. Upon maturation the ζ -potential of

CitOH-HA and Cit-HA samples does not change significantly, while Glr-HA becomes slightly more negative.

3.4. FT-IR characterization

FT-IR spectra of the carboxylate-HA samples are shown in Fig. 4A–C. All the most intense bands belong to apatitic phosphate group vibrations, that are the triply degenerated antisymmetric stretching mode ($\nu_3\text{PO}_4$) at ca. 1030 cm^{-1} with shoulders at 1046 and 1075 cm^{-1} , the symmetric stretching mode ($\nu_1\text{PO}_4$) at ca. 960 cm^{-1} , and the triply degenerated bending mode ($\nu_4\text{PO}_4$) at 602 , 574 (as a shoulder) and 562 cm^{-1} . The different form of $\nu_3\text{PO}_4$ band for the biphasic Glr-HA 5 m sample in comparison to the other Glr-HA samples is due to the superposition of HA $\nu_3\text{PO}_4$ peaks (ca. 1030 and 1090 cm^{-1}) with OCP $\nu_3\text{PO}_4$ peaks (1055 and 1075 cm^{-1}) [54].

All the samples also present the HA hydroxyl ions librational mode band at 631 cm^{-1} and the OH^- ions stretching mode band at 3567 cm^{-1} (Fig. 4D) [55]. νOH bands become progressively more evident upon maturation for all the samples, indicating that with the improvement of crystallinity more hydroxyl ions become part of the crystal structure. Furthermore, the crystallinity trend Glr-HA > Cit-HA > CitOH-HA is observed also for νOH bands intensity (Fig. 4D). The presence of structural and adsorbed water in the samples is evinced by a very broad band in the 3700 – 2500 cm^{-1} range (Fig. 4D) [56]. The intensity of this band follows the trend CitOH-HA > Cit-HA > Glr-HA and decreases upon maturation, in agreement with TGA data. The presence of carbonate ions in the samples was confirmed by the presence of a very weak carbonate band at ca. 870 cm^{-1} and by two weak bands at 1415 and 1455 cm^{-1} , suggesting a B-type carbonate doping (CO_3^{2-} ions substituting PO_4^{3-} ions) [56]. B-type carbonate doping was expected, because carbonate ions enter into crystal lattice as phosphate substituent when HA is prepared by wet precipitation in presence of CO_3^{2-} ions, whereas A-type carbonate doping (CO_3^{2-} ions substituting OH^- ions) is usually favored when HA is

thermally reacted in presence of CO_2 [57]. The bands of associated to carboxylate groups stretching modes are present between 1650 and 1350 cm^{-1} and are superimposed with an adsorbed water band (1640 cm^{-1}). The assignment of these bands was validated by analyzing the FT-IR spectra of the samples after annealing at $600\text{ }^\circ\text{C}$ where, according to TGA curves, the carboxylate is completely decomposed while the carbonate ions are still present. The IR spectra (Figure S4) collected on thermally annealed samples show that the bands at 1570 cm^{-1} and at 1640 cm^{-1} disappear or are very weak, confirming their assignment as asymmetric ν_{OCO} of carboxylates and ν_{water} , respectively. The bands at 1415 and 1455 cm^{-1} of the annealed samples are similar to the ones of the pristine spectra, confirming their assignment as ν_{OCO} of carbonate ions. In the same spectral range should fall also the symmetric ν_{OCO} of carboxylate ions, but these bands are covered by carbonate ν_{OCO} bands.

CitOH-HA IR spectra has more intense bands in the 1650 – 1350 cm^{-1} range in comparison to Cit-HA, which in turn are more intense than the Glr-HA samples (Fig. 4D). This confirms the trend CitOH-HA > Cit-HA > Glr-HA for carboxylate and structural water content measured through compositional analysis. Furthermore, the intensity of these bands decreases upon maturation for all the materials (Figure S5), confirming the decrease of carboxylate and water content with maturation. The IR spectra of Glr-HA is featured by a different position of carboxylate bands in comparison to Cit-HA and CitOH-HA, where the asymmetric ν_{OCO} of glutarate ions falls at 1632 and 1549 cm^{-1} . This discrepancy suggests that in Glr-HA the carboxylate molecule has a different binding geometry toward HA surface in comparison to Cit-HA and CitOH-HA, while Cit and CitOH have a similar geometry due to the matching of the respective peak position and shape.

3.5. Morphological characterization

The morphology of CitOH-HA, Glr-HA and Cit-HA nanoparticles was evaluated by FEG-SEM microscopy (Fig. 5 and S6). FEG-SEM image of

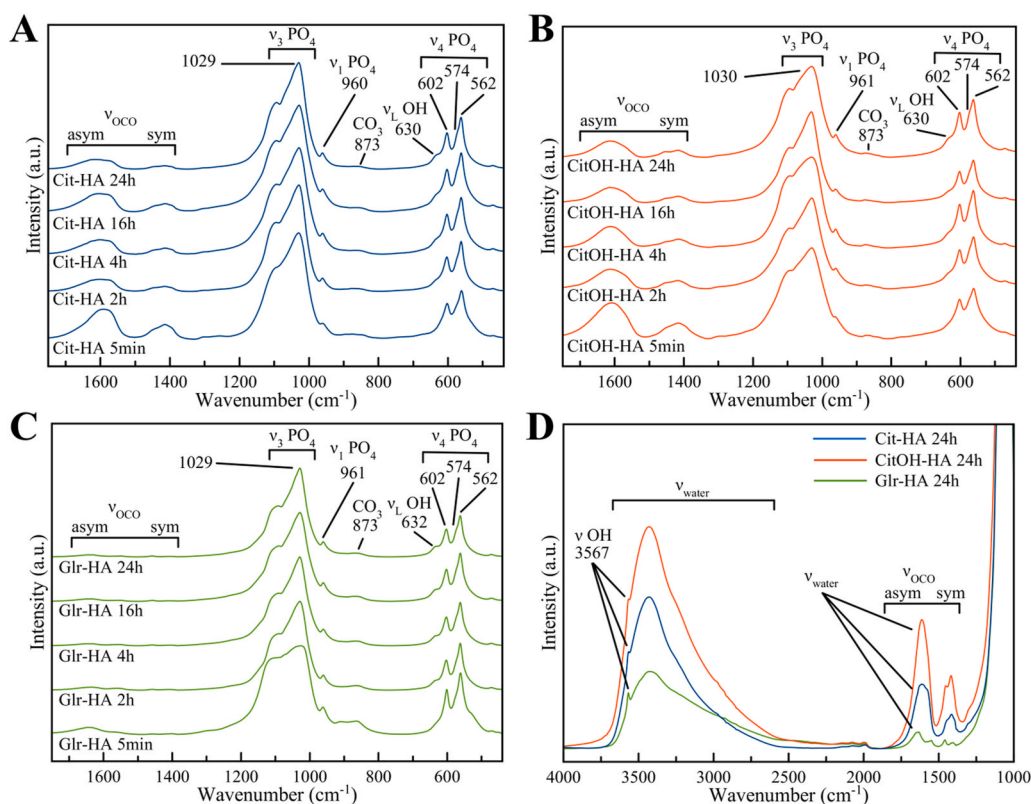


Fig. 4. FT-IR spectra of (A) Cit-HA, (B) CitOH-HA, and (C) Glr-HA at 5 m, 2h, 4h, 16h, 24h of maturation time. (D) 4000 – 1000 cm^{-1} spectral region of Cit-HA 24h, CitOH-HA 24 and Glr-HA 24h. Intensity of the spectra was normalized on $\nu_3\text{PO}_4$ band.

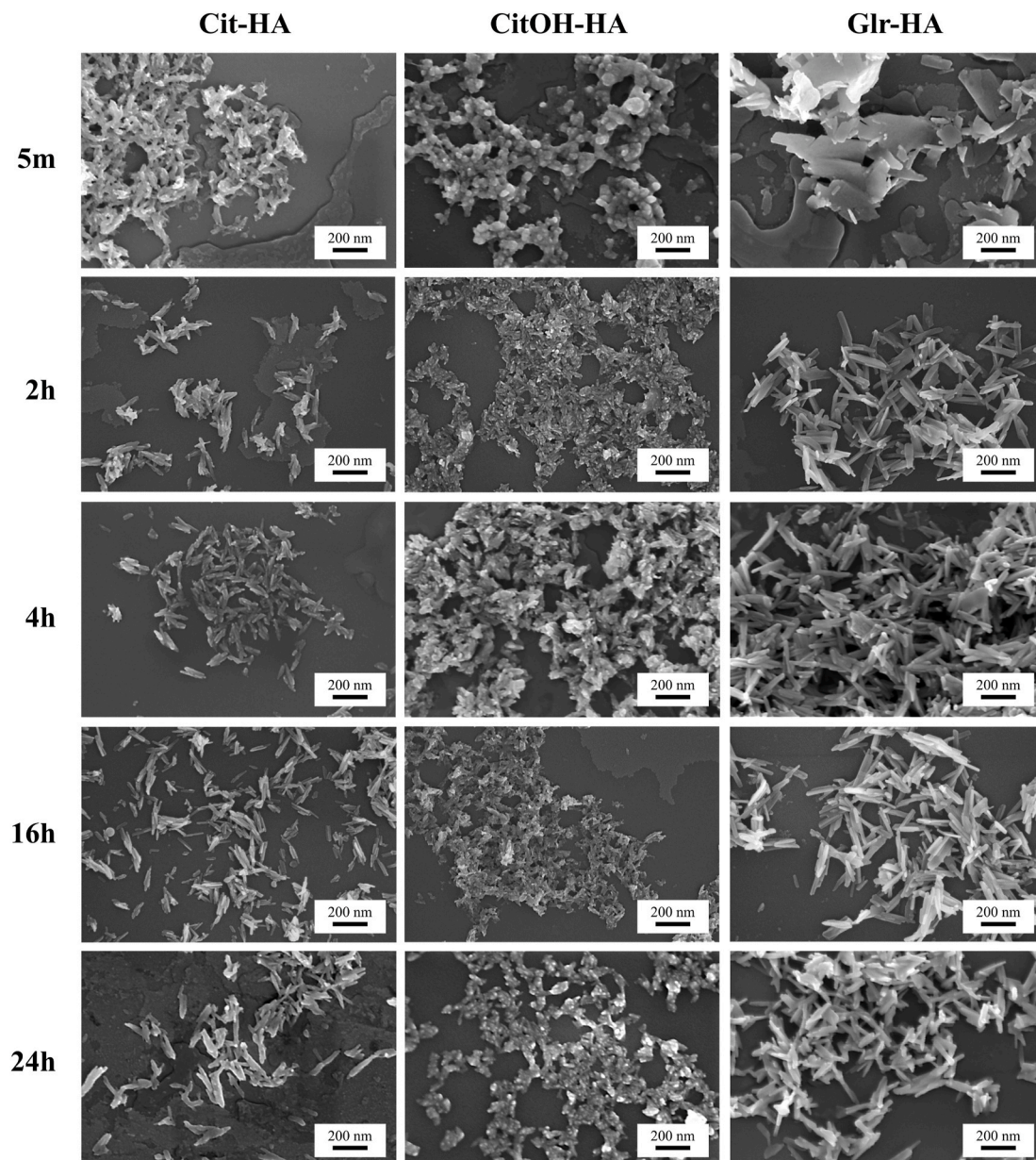


Fig. 5. FEG-SEM micrographs of Glr-HA, Cit-HA, and CitOH-HA nanoparticles prepared at different maturation times (magnification: 200000 \times).

the Glr-HA 5 m shows crystals with plate-like morphology having average length and width in the size ranges of 200–400 nm and 100–300 nm, respectively, and a thickness in the 10–20 nm range, mixed with elongated, rod-like crystals of ca. 100 nm in length and 10–20 nm in width. Along with the maturation time, in Glr-HA the plate-like particles disappear and only the rod-like ones are present, which grow in length and width reaching ca. 150 nm in length and 20–30 nm in width at 24h of maturation. The platelets found in Glr-HA 5 m were not observed in Cit-HA nor in CitOH-HA samples, neither in previous works on Cit-HA nanoparticles [18,24,58,59]. On the other hand, similar particles were reported for OCP crystals precipitated from aqueous solution [60–63]. In this view, it is likely that the platelets observed in Glr-HA 5 m are made of OCP and the rod-like crystals are made of HA. It is remarkable that the former crystals are smaller than OCP crystals precipitated in similar conditions without Glr (which can be several microns in size) [60–63], suggesting that Glr has partially inhibited OCP crystal growth and favored its conversion to HA. Previous works have proven that the conversion of OCP to HA occurs by an internal atomic rearrangement [60–62]. OCP conversion into HA is associated to a loss

of water and a rearrangement of HPO_4^{2-} ions that belong to the so-called “hydrated layer” of OCP unit cell, that is a layer that connect two regions of unit cell structurally similar to HA (called “apatitic layers”). During the conversion of OCP into HA, a structural stress is generated by the displacement of HPO_4^{2-} ions and water molecules and by the mismatch between the (100) crystal planes of OCP and HA. The consequence of the structural stress is the splitting of the apatitic layers across OCP crystal width. This generates slits that run along OCP main axis where single HA nanocrystals detach [60–62]. Morphology analysis suggests that it is likely that the same mechanism occurred in OCP conversion in Glr-HA. Therefore, the binding of Glr on OCP surface had a twofold action as (i) it inhibits further crystal growth, and (ii) favors the internal atomic rearrangement that is associated to the transformation of OCP crystal lattice into HA crystal lattice.

FEG-SEM micrographs of CitOH-HA 5 m show that the sample is constituted by small, irregular, isotropic nanoparticles with a diameter of ca. 30 nm. Along the maturation time the particles evolve into irregular and elongated nanoparticles with a length of 30–40 nm and a width of ca. 10 nm. The stronger growth inhibition effect of CitOH is

evident from FEG-SEM micrographs, since CitOH-HA nanoparticles are about 7 times smaller than Glr-HA and 2 times smaller than Cit-HA. In addition, at 5 m of maturation CitOH-HA nanoparticles have a round shape morphology that is common for very poorly crystalline calcium phosphate deriving from an amorphous precursor [64].

Previous works on Cit-HA crystallization have shown that Cit-HA evolves from very poorly crystalline particle aggregates to thin and platy elongated nanoparticles [18,53]. The FEG-SEM micrographs of Cit-HA samples are in agreement with the literature, where at 5 m of maturation Cit-HA consists of irregular, elongated nanoparticles of 70 nm in length and 30 nm in width. After maturation the particles have better-defined borders, and appear as flattened rods of about 80 nm in length and 30 nm in width.

The mean length (L) along the longest axis, the mean width (W) along the shortest axis, and the aspect ratio (R) of CitOH-HA, Glr-HA, and Cit-HA at 5 m and 24h of maturation were estimated from FEG-SEM images and are reported in Table 4. In the case of the isotropic particles of CitOH-HA 5 m, the mean diameter (D) is reported, while in the case of biphasic Glr-HA 5 m the dimensional parameters of both HA and OCP crystals are described. The particles mean dimensions were compared to the crystalline domains calculated from PXRD data. In agreement with PXRD data, the order Glr-HA > Cit-HA > CitOH-HA is respected also in terms of particle size. Furthermore, the increase of particle dimensions follows the same trend of the increase of crystalline domains, where Glr-HA and Cit-HA grew more than CitOH-HA with maturation time. In agreement with crystalline domains, all the samples present elongated particles with high R values, where the aspect ratio is similar for CitOH-HA and Cit-HA and is higher for Glr-HA after 24 h.

Samples were characterized by SAXS with synchrotron radiation. We took in consideration in our analysis only the experimental data that were less correlated to each other (Table S3-S5). For all data belonging to the same group (CitOH-HA, Glr-HA and Cit-HA), the agreement value (χ^2) was calculated by using the comparison function included into PRIMUS program [65] of the ATSAS package [40]. The selected data were those with the highest value of χ^2 . A preliminary analysis of the experimental SAXS curves was performed to evaluate the quality of the data and to obtain the basic structural information related to the size and shape of the nanoparticles. Such structural overall parameters are: (i) the radius of gyration (R_g), which is calculated from the slope of Guiner plot [66] and (ii) the maximum size of the nanoparticles (D_{max}) which can be obtained by means of the Pair-Distance Distribution Function [P(r)] by using the Indirect Fourier Transformation as described by Glatter et al. [67]. Both those parameters were evaluated by using AUTORG [68] and GNOM [69] programs of the ATSAS package [40], taking in consideration a monodisperse system, and they are reported in Table 5. Only from these two parameters the CitOH-HA samples seem to be very different from those of Cit-HA and Glr-HA, presenting smaller R_g and D_{max} . A better evaluation of the nanoparticles shape was obtained by fitting the experimental curves with different models, refining the model parameters and the associated polydispersity (Table 5 and Figure S7) by

Table 4

Mean length (L), mean width (W), their aspect ratio (R), and the mean diameter (D) of the samples.^a

Sample	L (nm)	W (nm)	R (nm)	D (nm)
Cit-HA 5 m	66 ± 19	25 ± 10	2.6	-
Cit-HA 24h	81 ± 24	27 ± 9	3.0	-
CitOH-HA 5 m	-	-	-	32 ± 8
CitOH-HA 24h	35 ± 10	12 ± 3	2.9	-
Glr-HA 5 m (OCP)	351 ± 99	185 ± 73	1.9	-
Glr-HA 5 m (HA)	125 ± 39	19 ± 5	6.6	-
Glr-HA 24h	148 ± 38	22 ± 8	6.7	-

^a Measured from FEG-SEM micrographs. Mean values and relative standard deviations were calculated from the measurement of at least 100 particles from different batches.

Table 5

SAXS data analysis: overall parameters in terms of gyration radius (R_g) and maximum size of the particle (D_{max}), and model parameters for lamellar and elliptical cylinder model, respectively. In the case of model fitting, the refined value of polydispersity (the ratio of standard deviation to the average value) associated to each parameter is reported in brackets.

Sample	Overall Parameters		Lamellar Model	Elliptical Cylinder Model		
	R_g (nm)	D_{max} (nm)	Thickness (nm)	R_{min} (nm)	Axis ratio (nm)	L (nm)
Cit-HA 5 m	14.2	44.5	4.8 (0.6)	17.0 (0.3)	1.98 (0.1)	3.7 (0.4)
Cit-HA 4h	13.9	44.3	3.7 (0.4)	27.7 (0.1)	1.2 (0.1)	3.8 (0.4)
Cit-HA 24h	16.3	48.5	3.9 (0.5)	22.0 (0.3)	1.5 (0.5)	3.1 (0.4)
CitOH-HA 5 m	7.8	24.0	ND	7.4 (0.1)	1.79 (0.1)	26.0 (0.5)
CitOH-HA 4h	7.8	24.6	ND	1.7 (0.1)	3.84 (0.1)	35.0 (0.1)
CitOH-HA 24h	7.4	23.5	ND	2.1 (0.2)	2.76 (0.1)	26.8 (0.1)
Glr-HA 5 m	15.8	48.3	12.1 (0.7)	6.4 (0.2)	2.73 (0.1)	46.3 (0.1)
Glr-HA 4h	12.9	36.9	4.7 (1.5)	4.0 (0.2)	4.5 (0.2)	27.6 (0.2)
Glr-HA 24h	12.6	36.7	6.4 (0.5)	3.5 (0.2)	4.3 (0.0)	30.1 (0.2)

using SasView program. The polydispersity for each of the refined parameter, reported in bracket near the numbers in Table 5, was evaluated as a ratio between the standard deviation and the mean value.

As first step, a simple lamellar model was used, which can give information only about the thickness of the nanoparticles. Two things were observed: (i) the curves of all CitOH-HA samples could not be fitted with a suitable lamellar model, and (ii) Cit-HA 5 m and Glr-HA 5 m samples are statistically different and thicker in comparison to the other samples. As second step, an elliptical cylinder model was used, which can give information about the shape as well as the size of nanoparticles [44]. In the elliptical cylinder model, the model parameters are: (i) L, that is the cylinder length, (ii) R_{min} , that is the minor radius of the elliptical base, and (iii) Axis ratio, that is the ratio between the major and the minor radius of the elliptical base. Indeed, the elliptical cylinder model shows that Cit-HA nanoparticles are disk-shaped (R_{min} ca. 17–27 nm, Axis ratio close to 1, L ca. 3–4 nm). These data are in good agreement with SEM morphology analysis (Table 6) and with literature [18,

Table 6

Comparison between dimensional parameters of the samples extracted by FEG-SEM and by SAXS. The values are: mean length (L), mean width (W), and the mean thickness (T).

Sample	FEG-SEM		SAXS ^a			Morphology
	L (nm)	W (nm)	L (nm)	W (nm)	T (nm)	
Cit-HA 5 m	66 ± 19	25 ± 10	67 ± 20	34 ± 10	3.7 ± 1.5	Elongated platy
Cit-HA 24h	81 ± 24	28 ± 9	66 ± 40	44 ± 15	3.1 ± 1.4	Elongated platy
CitOH-HA 5 m	32 ± 8 ^b	-	27 ± 4	26 ± 13	15 ± 2	Isotropic
CitOH-HA 24h	35 ± 10	12 ± 3	27 ± 3	12 ± 2	4.2 ± 0.8	Elongated platy
Glr-HA 5 m (HA)	125 ± 39	19 ± 5	n.d.	n.d.	n.d.	Rod
Glr-HA 24h	148 ± 38	22 ± 8	n.d.	n.d.	n.d.	Rod

^a Calculated from SAXS ellipsoidal cylinder model fitting.

^b The sample is isotropic, therefore the average of the diameter (D) is reported.

20,53], and confirm that Cit-HA nanoparticles have an elongated platy morphology. CitOH-HA samples also show good agreement between SEM morphological analysis and SAXS data modeling (Table 6), where CitOH-HA 5 m are composed of almost isotropic particles (although slightly flattened) while CitOH-HA 24h particles have an elongated platy morphology similar to Cit-HA. Differently, Glr-HA SAXS data modeling is discordant with SEM morphological analysis. It must be taken into account that the available q-range of SAXS data does not allow to measure particles that are bigger than ca. 100 nm, therefore Glr-HA nanoparticles lie outside this range at every maturation time. It is likely that in the elliptical cylinder modeling of Glr-HA the major dimensions of the particles are not detected, while the interparticle voids generate a difference of contrast that is included in the SAXS curve. Therefore, SAXS data modeling could not be performed for Glr-HA samples.

For selected SAXS data (i.e. Cit-HA 4h, and CitOH-HA 4h) we were able to obtain a three-dimensional model of the samples, by using the well-known ab-initio shape determination bead modeling approach (DAMMIF) [70]. In the bead modeling the nanoparticle is represented as a collection of a large number of densely packed beads inside a search volume, and each bead belongs either to the particle or to the solvent. DAMMIF utilizes the simulated annealing method to alter an arbitrary initial compact interconnected model in order to produce a calculated scattering pattern that fits the experimental SAXS data. With this approach, the shape of the nanoparticle is determined only by SAXS data fitting without any a priori guess of morphology, as in the case of SasView model fitting. The obtained bead models, as described above, are shown in Fig. 6 and in Supplementary Video 1. Bead models of all the samples tested confirmed the morphology and dimensions of the particles obtained by SasView (Tables 5 and 6), where all the samples are platy cylinders and Cit-HA is ca. twice bigger than CitOH-HA. Therefore, beads modeling confirms that Cit-HA, and CitOH-HA possess a platy cylinder morphology, and that elliptical cylinder is a suitable model for analyzing SAXS data of these nanoparticles.

Supplementary video related to this article can be found at <https://doi.org/10.1016/j.bioactmat.2021.01.010>

4. Conclusions

In this paper, we have studied the influence of three structurally similar calcium-binding carboxylate molecules on HA formation in terms of crystal growth, chemical composition and morphology. We have found that Cit, CitOH and Glr strongly influence HA crystallization with different effects even if they differ only for the central functional groups of the backbone structure. Cit-HA was used as comparison material, since it has been already extensively studied. CitOH strongly inhibits HA crystallization more efficiently than Cit. Even if they are composed of platy, elongated particles similar to those of Cit-HA, CitOH-HA nanoparticles are twice smaller and have a lower crystal order. The crystallization pathway of CitOH-HA is similar to Cit-HA, with the direct conversion from an amorphous precursor to HA.

On the other hand, Glr does not inhibit HA crystallization as Cit, but leads to the formation of OCP platelets that convert with maturation time to HA nanorods with larger aspect ratio than Cit-HA. Overall, in comparison to Cit-HA samples, Glr-HA nanoparticles have bigger dimensions, higher structural order, lower content of water and carboxylate ions, and lower surface charge. In addition, FT-IR data revealed that Glr has a different binding geometry and surface interaction toward HA in comparison to Cit and CitOH.

Our data demonstrate that crystallinity and particle dimensions of HA prepared in presence of Cit, CitOH and Glr are mainly controlled by the interaction strength of the carboxylate molecules with Ca^{2+} . Indeed, there is an inverse correlation between carboxylate- Ca^{2+} complex stability and HA size and crystallinity. Our data are in agreement with a previous computational modeling study on Cit-HA systems which has predicted that at low citrate concentration the HA growth is inhibited

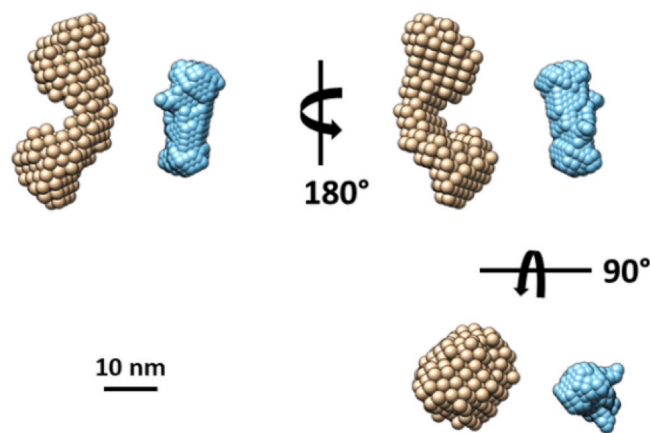


Fig. 6. SAXS bead ab-initio model for Cit-HA 4h (gold) and CitOH-HA 4h (blue).

generating small nanocrystals [23]. Moreover, the data of this paper allow to shed more light on the role of the chemical structure of Cit in regulating the HA morphology. Several papers ascribe this effect mainly to the spacing between the terminal carboxyl groups of Cit which matches the distance between the Ca^{2+} ions on the (1 0 0) HA crystal face, thus leading to a preferential binding of Cit toward this face and the inhibition of any further growth in this direction [18–21]. As a consequence, Cit-HA crystals grow along the directions orthogonal to the (1 0 0) crystal face leading to platy nanocrystals [17]. However, our results show that the length of the spacing between terminal carboxyl groups of the Cit is not a sufficient condition for generating the platy morphology, since Glr produces HA nano-rods even if Glr shares the same backbone structure of Cit. Differently, with CitOH the same morphology of Cit-HA has been achieved even if an additional hydroxyl group is present on the central region of molecule.

The presence of the additional hydroxyl group in CitOH leads to a stronger and more abundant binding of Ca^{2+} ions in solution first and to HA surface later, as proved by chemical composition analysis, but keeping the same preferential surface binding of Cit. Differently, the lack of the central carboxyl group of Glr does not only produce a weaker and less abundant binding to HA surface, but also has a less selective control on HA crystallization, forming rod-shaped HA nanoparticles. Therefore, these data reveal that the central carboxyl group of Cit does not only regulate the interaction strength with Ca^{2+} ions, but is also involved in the selective binding with HA crystal surface.

The results of this work highlight new possibilities to control the formation of HA for designing advanced bioactive materials with tailored physical-chemical properties. Future studies will focus in investigating the biological properties of carboxylate-HA nanoparticles as prepared and as sintered bioceramics.

CRediT authorship contribution statement

Lorenzo Degli Esposti: Investigation, Writing - original draft, Writing - review & editing, Funding acquisition. **Alessio Adamiano:** Investigation, Writing - review & editing. **Dritan Siliqi:** Investigation, Writing - review & editing. **Cinzia Giannini:** Investigation, Writing - review & editing. **Michele Iafisco:** Conceptualization, Writing - original draft, Writing - review & editing, Supervision.

Declaration of competing interest

The Authors declare no conflict of interest.

Acknowledgment

The authors acknowledge Dr. Heinz Amenitsch for the scientific and technical support during SAXS data collection.

Appendix A. Supplementary data

Supplementary data to this article can be found online at <https://doi.org/10.1016/j.bioactmat.2021.01.010>.

Funding

This work was supported by the CERIC-ERIC Consortium for financial support and for giving access to ELETTRA SAXS beamline (proposal CERIC-ERIC-20175403).

References

- [1] S.V. Dorozhkin, M. Epple, Biological and medical significance of calcium phosphates, *Angew. Chem. Int. Ed.* 41 (2002) 3130–3146, [https://doi.org/10.1002/1521-3773\(20020902\)41:17<3130::AID-ANIE3130>3.0.CO;2-1](https://doi.org/10.1002/1521-3773(20020902)41:17<3130::AID-ANIE3130>3.0.CO;2-1).
- [2] V. Rau Julieta, Antoniac Iulian, Cama Giuseppe, S. Komlev Vladimir, Ravaglioli Antonio, *Bioactive materials for bone tissue engineering*, *BioMed Res. Int.* 2016 (2016), <https://doi.org/10.1155/2016/3741428>.
- [3] M. Epple, K. Ganesan, R. Heumann, J. Klesing, A. Kovtun, S. Neumann, V. Sokolova, Application of calcium phosphate nanoparticles in biomedicine, *J. Mater. Chem.* 20 (2010) 18–23, <https://doi.org/10.1039/B910885H>.
- [4] V. Uskoković, S. Tang, M.G. Nikolić, S. Marković, V.M. Wu, Calcium phosphate nanoparticles as intrinsic inorganic antimicrobials: in search of the key particle property, *Biointerphases* 14 (2019), 031001, <https://doi.org/10.1116/1.5090396>.
- [5] G.B. Ramírez-Rodríguez, G. Dal Sasso, F.J. Carmona, C. Miguel-Rojas, A. Pérez-de-Luque, N. Masciocchi, A. Guagliardi, J.M. Delgado-López, Engineering biomimetic calcium phosphate nanoparticles: a green synthesis of slow-release multinutrient (NPK) nanofertilizers, *ACS Applied Bio Materials* 3 (2020) 1344–1353, <https://doi.org/10.1021/acsbam.9b00937>.
- [6] K. Mori, K. Yamaguchi, T. Hara, T. Mizugaki, K. Ebitani, K. Kaneda, Controlled synthesis of hydroxyapatite-supported palladium complexes as highly efficient heterogeneous catalysts, *J. Am. Chem. Soc.* 124 (2002) 11572–11573, <https://doi.org/10.1021/ja020444q>.
- [7] V.M. Wu, S. Tang, V. Uskoković, Calcium phosphate nanoparticles as intrinsic inorganic antimicrobials: the antibacterial effect, *ACS Appl. Mater. Interfaces* 10 (2018) 34013–34028, <https://doi.org/10.1021/acsami.8b12784>.
- [8] W. Wei, L. Yang, W. Zhong, J. Cui, Z. Wei, Poorly crystalline hydroxyapatite: a novel adsorbent for enhanced fulvic acid removal from aqueous solution, *Appl. Surf. Sci.* 332 (2015) 328–339, <https://doi.org/10.1016/j.apsusc.2015.01.209>.
- [9] J. Norton, K.R. Malik, J.A. Darr, I. Rehman, Recent developments in processing and surface modification of hydroxyapatite, *Advances in Applied Ceramics* 105 (2006) 113–139, <https://doi.org/10.1179/174367606X102278>.
- [10] K. Lin, C. Wu, J. Chang, Advances in synthesis of calcium phosphate crystals with controlled size and shape, *Acta Biomater.* 10 (2014) 4071–4102, <https://doi.org/10.1016/j.actbio.2014.06.017>.
- [11] M. Sadat-Shojai, M.-T. Khorasani, E. Dinpanah-Khoshdargi, A. Jamshidi, Synthesis methods for nanosized hydroxyapatite with diverse structures, *Acta Biomater.* 9 (2013) 7591–7621, <https://doi.org/10.1016/j.actbio.2013.04.012>.
- [12] J. Gómez-Morales, M. Iafisco, J.M. Delgado-López, S. Sarda, C. Drouet, Progress on the preparation of nanocrystalline apatites and surface characterization: overview of fundamental and applied aspects, *Prog. Cryst. Growth Charact. Mater.* 59 (2013) 1–46, <https://doi.org/10.1016/j.pcrysgrow.2012.11.001>.
- [13] J. Rau, I. Antoniac, M. Filipescu, C. Cotrut, M. Fosca, L. Nistor, R. Birjega, M. Dinescu, Hydroxyapatite coatings on Mg-Ca alloy prepared by pulsed laser deposition: properties and corrosion resistance in simulated body fluid, *Ceram. Int.* 44 (2018) 16678–16687, <https://doi.org/10.1016/j.ceramint.2018.06.095>.
- [14] S. Homaeigohar, T.-Y. Tsai, E.S. Zarie, M. Elbahri, T.-H. Young, A.R. Boccaccini, Bovine Serum Albumin (BSA)/polyacrylonitrile (PAN) biohybrid nanofibers coated with a biomimetic calcium deficient hydroxyapatite (HA) shell for wound dressing, *Mater. Sci. Eng. C* 116 (2020), 111248, <https://doi.org/10.1016/j.msec.2020.111248>.
- [15] A. Wang, H. Yin, D. Liu, H. Wu, M. Ren, T. Jiang, X. Cheng, Y. Xu, Size-controlled synthesis of hydroxyapatite nanorods in the presence of organic modifiers, *Mater. Lett.* 61 (2007) 2084–2088, <https://doi.org/10.1016/j.matlet.2006.08.019>.
- [16] J.A. Rincón-López, J.A. Herrmann-Muñoz, N. Cinca-Luis, L. López-Conesa, D.A. s. Fernández-Benavides, I. García-Cano, J.M. Guilemany-Casadamon, A. R. Boccaccini, J. Muñoz-Saldaña, J.M. Alvarado-Orozco, Apatite mineralization process from Silicocarnotite bioceramics: mechanism of crystal growth and maturation, *Cryst. Growth Des.* 20 (2020) 4030–4045, <https://doi.org/10.1021/acs.cgd.0c00322>.
- [17] Y.-Y. Hu, A. Rawal, K. Schmidt-Rohr, Strongly bound citrate stabilizes the apatite nanocrystals in bone, *Proc. Natl. Acad. Sci. Unit. States Am.* 107 (2010) 22425–22429, <https://doi.org/10.1073/pnas.1009219107>.
- [18] J.M. Delgado-López, M. Iafisco, I. Rodríguez, A. Tampieri, M. Prat, J. Gómez-Morales, Crystallization of bioinspired citrate-functionalized nanoapatite with tailored carbonate content, *Acta Biomater.* 8 (2012) 3491–3499, <https://doi.org/10.1016/j.actbio.2012.04.046>.
- [19] K. Chatzipanagis, M. Iafisco, T. Roncal-Herrero, M. Bilton, A. Tampieri, R. Kroger, J.M. Delgado-Lopez, Crystallization of citrate-stabilized amorphous calcium phosphate to nanocrystalline apatite: a surface-mediated transformation, *CrystEngComm* 18 (2016) 3170–3173, <https://doi.org/10.1039/C6CE00521G>.
- [20] J.M. Delgado-López, R. Frison, A. Cervellino, J. Gómez-Morales, A. Guagliardi, N. Masciocchi, Crystal size, morphology, and growth mechanism in bio-inspired apatite nanocrystals, *Adv. Funct. Mater.* 24 (2014) 1090–1099, <https://doi.org/10.1002/adfm.201302075>.
- [21] M. Iafisco, G.B. Ramírez-Rodríguez, Y. Sakhno, A. Tampieri, G. Martra, J. Gomez-Morales, J.M. Delgado-Lopez, The growth mechanism of apatite nanocrystals assisted by citrate: relevance to bone biomineralization, *CrystEngComm* 17 (2015) 507–511, <https://doi.org/10.1039/C4CE01415D>.
- [22] V. Bystrov, E. Paramonova, Y. Dekhtyar, A. Katashev, A. Karlov, N. Polyaka, A. Bystrova, A. Patmalnieks, A. Kholkin, Computational and experimental studies of size and shape related physical properties of hydroxyapatite nanoparticles, *J. Phys. Condens. Matter* 23 (2011), 065302, <https://doi.org/10.1088/0953-8984/23/6/065302>.
- [23] V. Bystrov, E. Paramonova, M. Costa, C. Santos, M. Almeida, S. Kopyl, Y. Dekhtyar, A. Bystrova, E. Maevsky, R. Pullar, A computational study of the properties and surface interactions of hydroxyapatite, *Ferroelectrics* 449 (2013) 94–101, <https://doi.org/10.1080/00150193.2013.822774>.
- [24] F.J. Martínez-Casado, M. Iafisco, J.M. Delgado-López, C. Martínez-Benito, C. Ruiz-Pérez, D. Colangelo, F. Oltolina, M. Prat, J. Gómez-Morales, Bioinspired citrate-apatite nanocrystals doped with divalent transition metal ions, *Cryst. Growth Des.* 16 (2015) 145–153, <https://doi.org/10.1021/acs.cgd.5b01045>.
- [25] J.M. Delgado-López, M. Iafisco, I. Rodríguez-Ruiz, J. Gómez-Morales, Bio-inspired citrate-functionalized apatite thin films crystallized on Ti-6Al-4V implants pre-coated with corrosion resistant layers, *J. Inorg. Biochem.* 127 (2013) 261–268, <https://doi.org/10.1016/j.jinorgbio.2013.04.004>.
- [26] K. Achelhi, S. Masse, G. Laurent, A. Saoiabi, A. Laghzizil, T. Coradin, Role of carboxylate chelating agents on the chemical, structural and textural properties of hydroxyapatite, *Dalton Trans.* 39 (2010) 10644–10651, <https://doi.org/10.1039/C0DT00251H>.
- [27] J. Chung, I. Granja, M.G. Taylor, G. Mpourmpakis, J.R. Asplin, J.D. Rimer, Molecular modifiers reveal a mechanism of pathological crystal growth inhibition, *Nature* 536 (2016) 446–450, <https://doi.org/10.1038/nature19062>.
- [28] M. Li, J. Zhang, L. Wang, B. Wang, C.V. Putnis, Mechanisms of modulation of calcium phosphate pathological mineralization by mobile and immobile small-molecule inhibitors, *J. Phys. Chem. B* 122 (2018) 1580–1587, <https://doi.org/10.1021/acs.jpcc.7b10956>.
- [29] Y.H. Tseng, Y. Mou, P.H. Chen, T.W. Tsai, C.I. Hsieh, C.Y. Mou, J.C. Chan, Solid-state P-31 NMR study of the formation of hydroxyapatite in the presence of glutaric acid, *Magn. Reson. Chem.* 46 (2008) 330–334, <https://doi.org/10.1002/mrc.2096>.
- [30] A. López-Macipe, J. Gómez-Morales, R. Rodríguez-Clemente, Nanosized hydroxyapatite precipitation from homogeneous calcium/citrate/phosphate solutions using microwave and conventional heating, *Adv. Mater.* 10 (1998) 49–53, [https://doi.org/10.1002/\(SICI\)1521-4095\(199801\)10:1<49::AID-ADMA49>3.0.CO;2-R](https://doi.org/10.1002/(SICI)1521-4095(199801)10:1<49::AID-ADMA49>3.0.CO;2-R).
- [31] J.P. Gustafsson, *Visual MINTEQ Version 3.0*, KTH, Dept. Of Land and Water Resources Engineering, Sweden, Stockholm, 2010.
- [32] J. Rodríguez-Carvajal, Recent advances in magnetic structure determination by neutron powder diffraction, *Physica B* 192 (1993) 55–69, [https://doi.org/10.1016/0921-4526\(93\)90108-1](https://doi.org/10.1016/0921-4526(93)90108-1).
- [33] J.M. Hughes, M. Cameron, K.D. Crowley, Structural variations in natural F, OH, and Cl apatites, *Am. Mineral.* 74 (1989) 870–876.
- [34] T. Ikoma, A. Yamazaki, S. Nakamura, M. Akao, Preparation and structure refinement of monoclinic hydroxyapatite, *J. Solid State Chem.* 144 (1999) 272–276, <https://doi.org/10.1006/jssc.1998.8120>.
- [35] K.J. Roche, K.T. Stanton, Measurement of fluoride substitution in precipitated fluorhydroxyapatite nanoparticles, *J. Fluor. Chem.* 161 (2014) 102–109, <https://doi.org/10.1016/j.jfluchem.2014.02.007>.
- [36] M. Espanol, J. Portillo, J.-M. Manero, M.-P. Ginebra, Investigation of the hydroxyapatite obtained as hydrolysis product of α -tricalcium phosphate by transmission electron microscopy, *CrystEngComm* 12 (2010) 3318–3326, <https://doi.org/10.1039/C001754J>.
- [37] C. Giannini, M. Ladisa, D. Altamura, D. Siliqi, T. Sibillano, L. De Caro, X-ray diffraction: a powerful technique for the multiple-length-scale structural analysis of nanomaterials, *Crystals* 6 (2016) 87, <https://doi.org/10.3390/cryst6080087>.
- [38] W. Wei, X. Zhang, J. Cui, Z. Wei, Interaction between low molecular weight organic acids and hydroxyapatite with different degrees of crystallinity, *Colloid. Surface. Physicochem. Eng. Aspect.* 392 (2011) 67–75, <https://doi.org/10.1016/j.colsurfa.2011.09.034>.
- [39] A. Hammersley, FIT2D: an introduction and overview, *European Synchrotron Radiation Facility Internal Report ESRF97HA02T* 68 (1997) 58.
- [40] D. Franke, M. Petoukhov, P. Konarev, A. Panjkovich, A. Tuukkanen, H. Mertens, A. Kikhney, N. Hajizadeh, J. Franklin, C. Jeffries, ATSAS 2.8: a comprehensive data analysis suite for small-angle scattering from macromolecular solutions, *J. Appl. Crystallogr.* 50 (2017) 1212–1225, <https://doi.org/10.1107/S1600576717007786>.
- [41] M. Kotlarchyk, S.H. Chen, Analysis of small angle neutron scattering spectra from polydisperse interacting colloids, *J. Chem. Phys.* 79 (1983) 2461–2469, <https://doi.org/10.1063/1.446055>.

- [42] M. Kotlarchyk, R.B. Stephens, J.S. Huang, Study of Schultz distribution to model polydispersity of microemulsion droplets, *J. Phys. Chem.* 92 (1988) 1533–1538, <https://doi.org/10.1021/j100317a032>.
- [43] F. Nallet, R. Laversanne, D. Roux, Modelling X-ray or neutron scattering spectra of lyotropic lamellar phases: interplay between form and structure factors, *J. Phys. II* 3 (1993) 487–502, <https://doi.org/10.1051/jp2:1993146>.
- [44] L. Feigin, D.I. Svergun, *Structure Analysis by Small-Angle X-Ray and Neutron Scattering*, Springer, Berlin, 1987.
- [45] M.A. Martins, C. Santos, M.M. Almeida, M.E.V. Costa, Hydroxyapatite micro-and nanoparticles: nucleation and growth mechanisms in the presence of citrate species, *J. Colloid Interface Sci.* 318 (2008) 210–216, <https://doi.org/10.1016/j.jcis.2007.10.008>.
- [46] J. Chung, R. Sosa, J.D. Rimer, Elucidating the effects of polyprotic acid speciation in calcium oxalate crystallization, *Cryst. Growth Des.* 17 (2017) 4280–4288, <https://doi.org/10.1021/acs.cgd.7b00608>.
- [47] A.E. Martell, R.M. Smith, *Critical Stability Constants*, Springer, Berlin, 1974.
- [48] G. Mitrofanova, Complexation of calcium ions with dicarboxylic acids in aqueous solutions, *Russ. J. Appl. Chem.* 75 (2002) 712–714, <https://doi.org/10.1023/A:1020385823712>.
- [49] S. Weiner, P.A. Price, Disaggregation of bone into crystals, *Calcif. Tissue Int.* 39 (1986) 365–375, <https://doi.org/10.1007/BF02555173>.
- [50] K. Tonsuaadu, K.A. Gross, L. Plüdduma, M. Veiderma, A review on the thermal stability of calcium apatites, *J. Therm. Anal. Calorim.* 110 (2011) 647–659, <https://doi.org/10.1007/s10973-011-1877-y>.
- [51] C. Rey, C. Combes, C. Drouet, H. Sfihi, A. Barroug, Physico-chemical properties of nanocrystalline apatites: implications for biominerals and biomaterials, *Mater. Sci. Eng. C* 27 (2007) 198–205, <https://doi.org/10.1016/j.msec.2006.05.015>.
- [52] V. Di Mauro, M. Iafisco, N. Salvarani, M. Vacchiano, P. Carullo, G.B. Ramírez-Rodríguez, T. Patrício, A. Tampieri, M. Miragoli, D. Catalucci, Bioinspired negatively charged calcium phosphate nanocarriers for cardiac delivery of MicroRNAs, *Nanomedicine* 11 (2016) 891–906, <https://doi.org/10.2217/nmm.16.26>.
- [53] P. Ivanchenko, J.M. Delgado-López, M. Iafisco, J. Gómez-Morales, A. Tampieri, G. Martra, Y. Sakhno, On the surface effects of citrates on nano-apatites: evidence of a decreased hydrophilicity, *Sci. Rep.* 7 (2017), 8901, <https://doi.org/10.1038/s41598-017-09376-x>.
- [54] B. Fowler, E. Moreno, W. Brown, Infra-red spectra of hydroxyapatite, octacalcium phosphate and pyrolysed octacalcium phosphate, *Arch. Oral Biol.* 11 (1966) 477–492, [https://doi.org/10.1016/0003-9969\(66\)90154-3](https://doi.org/10.1016/0003-9969(66)90154-3).
- [55] S. Koutsopoulos, Synthesis and characterization of hydroxyapatite crystals: a review study on the analytical methods, *J. Biomed. Mater. Res.* 62 (2002) 600–612, <https://doi.org/10.1002/jbm.10280>.
- [56] A. Antonakos, E. Liarokapis, T. Leventouri, Micro-Raman and FTIR studies of synthetic and natural apatites, *Biomaterials* 28 (2007) 3043–3054, <https://doi.org/10.1016/j.biomaterials.2007.02.028>.
- [57] H. Madupalli, B. Pavan, M.M. Tecklenburg, Carbonate substitution in the mineral component of bone: discriminating the structural changes, simultaneously imposed by carbonate in A and B sites of apatite, *J. Solid State Chem.* 255 (2017) 27–35, <https://doi.org/10.1016/j.jssc.2017.07.025>.
- [58] J. Gómez Morales, R. Fernández Penas, C. Verdugo-Escamilla, L. Degli Esposti, F. Oltolina, M. Prat, M. Iafisco, J. Fernández Sánchez, Bioinspired mineralization of type I collagen fibrils with apatite in presence of citrate and europium ions, *Crystals* 9 (2019) 13, <https://doi.org/10.3390/cryst9010013>.
- [59] J. Gómez-Morales, C. Verdugo-Escamilla, R. Fernández-Penas, C.M. Parra-Milla, C. Drouet, F. Maube-Bosc, F. Oltolina, M. Prat, J.F. Fernández-Sánchez, Luminescent biomimetic citrate-coated europium-doped carbonated apatite nanoparticles for use in bioimaging: physico-chemistry and cytocompatibility, *RSC Adv.* 8 (2018) 2385–2397, <https://doi.org/10.1039/C7RA12536D>.
- [60] J. Zhan, Y.H. Tseng, J.C. Chan, C.Y. Mou, Biomimetic formation of hydroxyapatite nanorods by a single-crystal-to-single-crystal transformation, *Adv. Funct. Mater.* 15 (2005) 2005–2010, <https://doi.org/10.1002/adfm.200500274>.
- [61] Y.-H. Tseng, C.-Y. Mou, J.C. Chan, Solid-state NMR study of the transformation of octacalcium phosphate to hydroxyapatite: a mechanistic model for central dark line formation, *J. Am. Chem. Soc.* 128 (2006) 6909–6918, <https://doi.org/10.1021/ja060336u>.
- [62] M. Iijima, H. Kamemizu, N. Wakamatsu, T. Goto, Y. Doi, Y. Moriwaki, Transition of octacalcium phosphate to hydroxyapatite in solution at pH 7.4 and 37 °C, *J. Cryst. Growth* 181 (1997) 70–78, [https://doi.org/10.1016/S0022-0248\(97\)00230-3](https://doi.org/10.1016/S0022-0248(97)00230-3).
- [63] M. Iafisco, J.G. Morales, M.A. Hernández-Hernández, J.M. García-Ruiz, N. Roveri, Biomimetic carbonate-hydroxyapatite nanocrystals prepared by vapor diffusion, *Adv. Eng. Mater.* 12 (2010) B218–B223, <https://doi.org/10.1002/adem.201080003>.
- [64] M. Iafisco, L. Degli Esposti, G.B. Ramírez-Rodríguez, F. Carella, J. Gómez-Morales, A.C. Ionescu, E. Brambilla, A. Tampieri, J.M. Delgado-López, Fluoride-doped amorphous calcium phosphate nanoparticles as a promising biomimetic material for dental remineralization, *Sci. Rep.* 8 (2018), 17016, <https://doi.org/10.1038/s41598-018-35258-x>.
- [65] P.V. Konarev, V.V. Volkov, A.V. Sokolova, M.H. Koch, D.I. Svergun, PRIMUS: a Windows PC-based system for small-angle scattering data analysis, *J. Appl. Crystallogr.* 36 (2003) 1277–1282, <https://doi.org/10.1107/S0021889803012779>.
- [66] A. Guinier, La diffraction des rayons X aux très petits angles : application à l'étude de phénomènes ultramicroscopiques, *Ann. Phys.* 11 (1939) 161–237, <https://doi.org/10.1051/anphys/193911120161>.
- [67] O. Glatter, A new method for the evaluation of small-angle scattering data, *J. Appl. Crystallogr.* 10 (1977) 415–421, <https://doi.org/10.1107/S0021889877013879>.
- [68] M.V. Petoukhov, P.V. Konarev, A.G. Kikhney, D.I. Svergun, ATSAAS 2.1—towards automated and web-supported small-angle scattering data analysis, *Applied Crystallography* 40 (2007) s223–s228, <https://doi.org/10.1107/S0021889807002853>.
- [69] D. Svergun, Determination of the regularization parameter in indirect-transform methods using perceptual criteria, *J. Appl. Crystallogr.* 25 (1992) 495–503, <https://doi.org/10.1107/S0021889892001663>.
- [70] D. Franke, D.I. Svergun, DAMMIF, a program for rapid ab-initio shape determination in small-angle scattering, *J. Appl. Crystallogr.* 42 (2009) 342–346, <https://doi.org/10.1107/S0021889809000338>.
- [71] H. Amenitsch, M. Rappolt, M. Kriechbaum, H. Mío, P. Laggner, S. Bernstorff, First performance of the small-angle X-ray scattering beamline at ELETTRA, *J. Synchrotron Radiat.* 5 (1998) 506–508, <https://doi.org/10.1107/S090904959800137X>.
- [72] G. Porod, O. Glatter, O. Kratky, *Small Angle X-ray Scattering*, Academic Press, London, 1982.